

Significant tuning of internal mode coupling in doubly clamped MEMS beam resonators by thermal effect

Chao Li¹, Qian Liu¹, Kohei Uchida¹, Hua Li², Kazuhiko Hirakawa³, and Ya Zhang^{1a)}

¹*Institute of Engineering, Tokyo University of Agriculture and Technology, Koganei-shi, Tokyo,
184-8588, Japan*

²*Shanghai Institute of Microsystem and Information Technology, Chinese Academy of Sciences,
Shanghai 200050, China*

³*Institute of Industrial Science, University of Tokyo, 4-6-1 Komaba, Meguro-ku, Tokyo 153-
8505, Japan*

Abstract

Intermodal coupling has been demonstrated to be a promising mechanism for the development of advanced micro/nanoelectromechanical devices. However, strong mode coupling remains a key challenge limiting the practical application of intermodal coupling. Furthermore, the insight into physical mechanisms underlying mode coupling and the capability to quantitatively tune the mode coupling is also limited. Here, we experimentally and theoretically demonstrate the significant tunability of mode coupling by using the thermal tuning effect, yet in an asymmetric doubly-clamped MEMS beam resonator, enabling various coupling strength to be implemented for practical applications. In this system, two out-of-plane vibrational modes are mechanically coupled through displacement-induced tension, and their mode coupling strength arises from both hardening and softening nonlinearities of the two modes, thus allowing for the tuning of mode coupling strength by thermally enhancing the softening nonlinearity of the MEMS beam. Our results demonstrate a

feasible approach to tune the mode coupling and offer insights into fundamental mechanism of mode coupling in MEMS beam resonators, paving the way for the development of MEMS resonators with enhanced performance and application-specific tunability.

a) Electronic mail: zhangya@go.tuat.ac.jp

Introduction

Interactions among two or more vibrational modes in micro/nanoelectromechanical systems (M/NEMS) resonators have been a growing interest in the past decade or so, and have been engineered into special gain mechanisms used for frequency locking¹⁻³, synchronized oscillation⁴⁻⁶, signal amplification^{7,8}, energy dissipation⁹⁻¹¹, and highly-sensitive sensing¹²⁻¹⁵. Among the above mode interactions, one remarkable category belongs to intermodal coupling, where two or more mechanical resonators are coupled via phonon cavity¹⁶⁻¹⁹, or two or more vibrational modes in a single resonator are nonlinearly coupled²⁰⁻²². Different from internal resonance that occurs at the specific frequency condition^{23,24}: the frequencies of two engaged modes fulfill or nearly fulfill with an integer ratio of N , intermodal coupling can couple any two modes without elaborate geometric design for realizing the prerequisite relationship of their frequencies. This gives an advantage of bridging distinct mechanical modes easier and achieving more reliable information transfer. However, when two internally coupled modes are not commensurate with an integer frequency ratio, the energy exchange is rather modest in comparison to the case of internal resonance, which makes it difficult to achieve strong intermodal coupling. Control on mode coupling in M/NEMS resonators remains a key challenge limiting practical applications of intermodal coupling as well.

Here, we demonstrate the significant tunability of mode coupling in an asymmetric doubly-clamped MEMS resonator using the thermal tuning effect. In this system, two out-of-plane vibrational modes are mechanically coupled through the displacement-induced tension, and the tuning of mode coupling strength (i.e., mode coupling coefficient) is achieved by thermally inducing the softening nonlinearity of the MEMS beam. Although mode coupling mechanisms based on the geometric nonlinearity or the displacement-induced tension in M/NEMS resonators have been reported in the past studies^{21,22,25-27}, these studies so far have mostly concentrated on experimental observations, applications and characterization. Investigations regarding the quantitative tuning of mode coupling

strength and the physical origins of tunability are less touched, and the interaction mechanism between coupling and nonlinearity is also unclear. Furthermore, manufacturing defects and small asymmetries (e.g., initial bending) can have a huge impact in such systems, thus, the ability to determine coupling strength by geometric design remains limited and is often elusive. We here present a general theoretical model integrated with strain tuning and asymmetries to quantitatively describe the mode coupling coefficient. It is shown that mode coupling coefficient arises from both the hardening and softening nonlinearities of the two vibrational modes. This mechanism is akin to the case of a single vibration mode that the hardening and softening nonlinearities jointly determine the total nonlinearity. From a more essential perspective, both nonlinearity and mode coupling coefficient originate from the change in stiffness caused by the extension of the beam in vibration, suggesting that there is a direct link between nonlinearity and mode coupling coefficient. Moreover, this model provides valuable insight for achieving various coupling strengths in beams, allowing strong and weak coupling to be implemented in applicable applications.

Results

Characterization of mode coupling coefficient

For a doubly clamped MEMS beam, mechanical mode coupling between out-of-plane modes usually appears as: when a mode is excited, the resonance frequency of a second mode gets tuned^{21,22}. This is because oscillation of the excited mode provides additional tension along the beam axis, thereby changing the effective stiffness of the beam, which in turn modulates the resonance frequency of all vibrational modes. This frequency modulation depends for each mode on its coupling coefficient to the excited mode and the oscillation amplitude of the excited mode. We call the 1st excited mode as pump mode, or mode- j , and the 2nd mode which shows the frequency shift as the

probe mode, or mode- k in this work. Then, such coupling behavior can be formulated by (see Eq. (23) in the Section of Materials and methods)

$$\Delta f = f_k' - f_k = f_k \lambda_{kj} a_j^2, \quad (1)$$

where a_j indicates the oscillation amplitude of mode- j , f_k' and f_k are the resonance frequencies of mode- k with and without the excitation of mode- j , respectively. λ_{kj} is the mode coupling coefficient between mode- k and mode- j , enabling the oscillation of mode- j to convert into frequency shift of mode- k . We have derived an analytic expression of λ_{kj} as (see more details in the subsection of Theoretical model)

$$\lambda_{kj} = \frac{EW_{kk}W_{jj}}{8\rho L^4 \omega_k^2} - \frac{3x_T^2 E^2 W_{jj} W_{kk} W_{0k}^2}{8\rho^2 L^8 \omega_k^4} = \frac{A}{\omega_k^2} - \frac{x_T^2}{\omega_k^4} B, \quad (2)$$

where A and B represent the constant parts during the calculation of λ_{kj} , and $\omega_k = 2\pi f_k$. Eq. (2) indicates that λ_{kj} highly depends on the center deflection of the MEMS beam, x_T and f_k . In our previous research²⁸, we have reported that both x_T and f_k can be efficiently modulated by applying a thermal strain to the MEMS beam, which can reduce the mechanical nonlinearity of the MEMS beam. Here, we show that the thermal effect also enables the significant tuning of the internal mode coupling strength in the MEMS beam resonator. The measured mode coupling strength λ_{kj} following Eq. (1) agrees well with the theoretical value calculated by Eq. (2), demonstrating our method a feasible approach to tune the mode coupling, as well as offering insights into fundamental mechanism of mode coupling in MEMS beam resonators.

Thermal tuning of mode coupling coefficient in GaAs doubly clamped beam resonators

Our mode coupling tuning measurement was performed on GaAs doubly clamped MEMS beam

resonators^{29–31}. A microscope image of the doubly-clamped MEMS beam resonator is shown in Fig. 1(a), which is fabricated by using a modulation-doped (Al, Ga)As/GaAs heterojunction grown by molecular-beam epitaxy³² (see more fabrication details in “ Materials and methods” section). The measurement system consists of a laser Doppler vibrometer (LDV) and a lock-in amplifier with a built-in phase locked loop (PLL). We drive the beam into oscillation by applying an ac voltage (V_D) to one of the piezoelectric capacitors (C_1 or C_2) and then measured the beam oscillation by the LDV and a lock-in amplifier with a built-in PLL. All the measurements were performed in a vacuum ($\sim 10^{-4}$ Torr) at room temperature.

Figure 1(b) plots the measured oscillation spectrum from 0.1–0.8 MHz using open-loop sweep, with a driving voltage of $V_D = 100$ mV. As seen, the first three vibrational modes are obtained, they are 1st bending mode (235.5 kHz), 2nd bending mode (644.5 kHz) and 1st torsional mode (752 kHz), respectively, whose mode shapes are shown by the inset of Fig. 1(b). Here, we utilize the two bending modes (i.e., out-of-plane modes) to study their mode coupling, and furthermore apply thermal strain to tuning the mode coupling strength. The out-of-plane modes are selected rather than the in-plane modes (i.e., torsional modes) because they are more sensitive to the tension along the beam axis^{21,27}, thus can be efficiently tuned by the thermal strain.

We applied a DC voltage (V_{NiCr}) to the NiCr heater (see Fig. 1(a)) to induce thermal strain in the beam. The electrothermal heating induces a temperature rise in the MEMS beam and causes the beam to expand along the beam axis thermally. Since the two ends of the beam are fixed, a compressive strain is generated in the beam. With the input heat, the resonance frequency, ω_k , of the MEMS beam is modulated. Figure 1(c) shows the measured resonance frequencies of the 1st bending mode (blue) and the 2nd bending mode (red) as a function of heating power, P . As seen, for the case of the 1st

bending mode, the resonance frequency first decreases with heating power until $P = 1.33$ mW, and then starts to increase with the further increased heating power, suggesting the 1st bending mode enters its buckling domain. For an ideally straight beam, the bending moment and the flexural rigidity cancel each other out at the buckling point, giving a zero resonance frequency for the bending mode. In experiments, however, since there is always a small initial center deflection, x_0 , in the MEMS beam from the mesa structure of the MEMS beam, the resonance frequency normally does not drop to zero, as we have clarified in previous publications^{28,29}. Nevertheless, the center deflection of the MEMS beam sharply increases as P exceeds the buckling point ($P = 1.33$ mW), inducing an increase in the resonance frequency of the 1st bending mode. The initial center deflection, x_0 , can be determined by the resonance frequency shift with applied heating power, as we have demonstrated in our previous study²⁸. In this work, we have calibrated that $x_0 \approx 100$ nm (see Appendix B for more details), which plays an important role in building an accurate mode coupling model for the initially curved MEMS beam. For the 2nd bending mode, the frequency keeps decreasing with the heating power, and the buckling is not yet achieved with the currently applied heating power.

To study the effect of thermal tuning on the mode coupling between two vibrational modes, we drive the 1st bending mode in the self-sustained oscillation mode with the PLL³³, which we employed as the probe mode in this work. The PLL compensates the energy loss of the probe mode through feedback control, thus maintains the oscillation amplitude as well as track the resonance frequency of the probe mode (f_k)²¹. The 2nd bending mode is employed as the pump mode, and when it is driven into oscillation with an oscillation amplitude a_j , the probe mode shows a shift in its resonance frequency (f_k). The measured a_j and f_k are used to estimate the mode coupling coefficient, λ_{kj} , with Eq. (1).

Figure 2(a-c) shows the oscillation spectra of the pump mode (red) and the corresponding resonance frequency of the probe mode (blue) when the pump mode is excited, at various heating powers, P , where the x-axis plots the driving frequency of the pump mode (f_j), the left y-axis plots the resonance frequency (f_k) of the probe mode tracked by PLL, and the right y-axis plots the squared amplitude of the pump mode (a_j^2). As seen from Fig. 2(a), the f_k changes with the a_j^2 , and always shifts to the higher frequency side. The change in f_k is obviously proportion to the a_j^2 , which is consistent with Eq. (1), indicating the existence of the mechanical mode coupling. Furthermore, the blue shift in f_k indicates that the coupling coefficient is a positive value under this condition ($P = 0$ mW). However, when the heating power increases to 1.35 mW as shown in Fig. 2(b), the f_k exhibits a small back-and-forth oscillation near the resonance frequency of the probe mode, i.e., the oscillation of the pump mode barely affects the f_k , indicating the coupling coefficient is rather tiny (~ 0). Furthermore, when the heating power reaches 1.58 mW as shown in Fig. 2(c), the f_k starts to shift to the lower frequency side during the excitation of the pump mode and the frequency changes in f_k are negatively in proportion to the a_j^2 , suggesting that the coupling coefficient becomes negative under this condition. The above results of the mode coupling measurement demonstrate that the mode coupling coefficient between the pump and probe modes can be largely tuned by the input heat to the MEMS beam.

To further quantitatively characterize and intuitively visualize the tunability of the mode coupling coefficient, we estimate the mode coupling coefficient, λ_{kj} , by performing linear fitting with Eq. (1); the data is from the resonance spectra of the pump mode and the resonance frequency of the pump mode, at various heating powers, as exemplified by Figs. 2(a-c). To take an example, Figure 3 (a) plots the f_k as a function of a_j^2 for the case of $P = 0$ mW. As seen, f_k and a_j^2 have a good linear relationship, enabling the calculation of λ_{kj} by dividing the slope of the plot by the y-intercept (corresponding to the resonance frequency when $a_j = 0$). Figures 3(b) shows both the experiment (dots)

and calculation (line) results of the λ_{kj} as a function of heating power. As seen, the calculated λ_{kj} using Eq. (2) shows nice agreement with the experimental λ_{kj} , and both have well shown a significant tuning with heating power P .

As seen from Fig. 3(b), the λ_{kj} first experiences a slight rise as the heating power increases from zero. This can be understood from the fact that the resonance frequency is quickly reduced as the P increases, whereas the increase in the center deflection, x_T , is rather slow before the buckling point. With further increased P approaching the buckling point, λ_{kj} drops rapidly to negative values, which is because x_T increases rapidly at the buckling point and governs the sharp reduction of λ_{kj} . It is worth noting that there exists a point that $\lambda_{kj} = 0$, indicating that the two modes decoupled from each other under this condition, showing the potential in the applications that require two modes vibrating independently. In the post-buckling regime, λ_{kj} shows a gentle change ($P > 1.8\text{mW}$). This is because although x_T still increases with P , the resonance frequency of the probe mode also increases rapidly, giving an almost stable λ_{kj} in the post-buckling regime.

Furthermore, we observed an interesting sudden drop in the experimental λ_{kj} when the resonance frequencies of the pump mode and probe mode fulfill an integer ratio $f_j : f_k = 3:1$, as indicated by the dotted black rectangle in Fig. 3(b), The blow-up of the corresponding part is shown in the inset of the figure. This is a typical internal resonance condition with an integer frequency ratio between two vibration modes^{31,34-36}. At this point, the coherent energy transfer between two modes through the 3rd order nonlinearity of the lower frequency mode is formed, causing the complex dynamics in the oscillation amplitude change and resonance frequency shift. Once the 3:1 mode coupling is excited, the pump mode draws vibrational energy from the probe mode², resulting in a sudden increase in the oscillation amplitude of the pump mode (see Appendix C for more details). Since the experimental λ_{kj} is obtained by linear fitting using Eq. (1), the suddenly increased oscillation amplitude of the pump

mode gives a drop in the λ_{kj} at the 3:1 mode coupling point.

Theoretical analysis

To figure out the physical origin of mode coupling coefficient, we developed a theoretical model for the present doubly-clamped MEMS beam resonator as schematically shown in Fig. 4(a). We start from the Euler-Bernoulli equation to derive the motion equation of the doubly-clamped MEMS beam, by assuming that two modes, i.e., 1st and 2nd bending modes (mode- k and mode- j) are excited simultaneously. Then the resonance frequency of the probe mode (f_k) is calculated as a function of the oscillation amplitude of the pump mode (a_j), from which we obtain the mode coupling coefficient, λ_{kj} , (See Eq. (22) in the Section of Materials and methods). The derived λ_{kj} exhibits tunability since the center deflection and internal strain in the beam were considered in the model, which is different from the ones provided in Refs.^{21,27}, Furthermore, we have noticed that the measured λ_{kj} shows a very similar trend with the mechanical nonlinearity change which we have reported in a previous work²⁸, indicating that mode coupling and nonlinearity may be highly correlated. Therefore, we also derived the nonlinearities of the probe and pump modes ($\alpha_{2j,k}$ and $\alpha_{3j,k}$), which can be found in the subsection of theoretical model.

From the results shown above, we have found that the mode coupling coefficient can be directly linked to the mechanical nonlinearities of the pump and probe modes, as

$$\lambda_{kj} = \frac{\sqrt{\alpha_{3k} \times \alpha_{3j}}}{4\omega_k^2} - \frac{\alpha_{2k}^2 W_{jj}}{6\omega_k^4 W_{kk}}, \quad (3)$$

where α_{3j} , α_{3k} are the 3rd order (cubic) nonlinearity coefficients for the pump and probe modes, α_{2k} is the 2nd order (quadratic) nonlinearity coefficient, ω_k is the resonance frequency of the probe mode, W_{jj} and W_{kk} are the mode overlapping parameters determined by the mode shapes (mode- j and mode- k), respectively. Thus, we have concluded that the mode coupling coefficient discussed in

this work is fully determined by the mechanical nonlinearities of the two coupled vibrational modes, and its tunability is from the tunable mechanical nonlinearities of two coupled modes. This can be understood that both the mechanical nonlinearity and the mode coupling coefficient discussed here originate from the change in stiffness caused by the extension of the beam in vibration, thus are highly correlated with each other.

To quantitatively calculate λ_{kj} , the simplified 1-dimensional mode shapes for the 1st and 2nd bending modes (ϕ_k and ϕ_j) reported in previous literature are utilized, as³⁷,

$$\phi_k = 1.01781 \cos[4.73004u] - 1.01781 \cosh[4.73004u] - \sin[4.73004u] + \sinh[4.73004u] \quad (4)$$

$$\phi_j = 0.999223 \cos[7.8532u] - 0.999223 \cosh[7.8532u] - \sin[7.8532u] + \sinh[7.8532u], \quad (5)$$

where u is the coordinate along the length of the beam. The mode shapes calculated with Eq. (4) and Eq. (5) can be found in the upper insets of Fig. 4(a). The numerical analysis starts with the MEMS beam resonators with dimensions of $133 \mu\text{m}(L) \times 27 \mu\text{m}(b) \times 1 \mu\text{m}(h)$ and with $E=85.9 \text{ GPa}$, $\rho=5307 \text{ kg/m}^3$ employed as the Young's modulus and density of GaAs material, which is consistent to the actual values in the sample. Figure 4 (b) plots the calculated λ_{kj} as a function of normalized strain, $\varepsilon/\varepsilon_{cr}$, at various normalized initial center deflections, x_0/h (h is thickness of the beam), in which ε represents the compressive strain induced by the applied heating power, and ε_{cr} is Euler's buckling critical strain of the MEMS beam. As seen, for various cases of x_0 , the λ_{kj} can be significantly tuned from positive to negative as the applied strain increases, indicating the feasibility of using thermal effect for controlling the mode coupling strength in MEMS beam. Furthermore, the results show that the change of mode coupling strength highly relies on the initial center deflection. It is of great interest that, the λ_{kj} can be tuned more significantly with a smaller x_0 . This is generally owing to the fact that the center deflection and the resonance frequency of the probe mode tend to change more dramatically

at small x_0 , giving more significant tuning in λ_{kj} . Figure 4(c) shows the absolute maximum in the mode coupling coefficient ($|\lambda_{kj}^{max}|$) that can be achieved using thermal tuning as a function of x_0/h . As seen, $|\lambda_{kj}^{max}|$ increases greatly with the decreasing x_0 , enabling the potential in application that needs ultra-strong coupling of vibrational modes.

Discussion and Conclusion

In this study, we experimentally and theoretically demonstrated the thermal tuning of the mode coupling coefficient in doubly clamped MEMS beam resonators. The tunability of the mode coupling coefficient is promising for applications that require either ultra-strong or weak coupling between vibrational modes in MEMS resonators. One example is to increase the detectable capability of vibration modes in MEMS resonators by intermodal coupling^{22,27}. With internal mode coupling, the vibration of higher-order modes can be probed with the resonance frequency shift of lower-frequency mode, in which the detection capability relies on the mode coupling coefficient between the two modes. Tuning the mode coupling coefficient is, therefore, an effective approach to improve the readout strength of high-frequency modes. This is in particularly important with the scaled NEMS resonators, of which the high-frequency modes commonly have very high resonance frequencies that are difficult to be detected with conventional methods. Another potential application is to achieve multimode sensing using two vibrational modes without cross-talk. Multimode sensors employing two or more vibrational modes enable simultaneous detection of different physical stimulus^{38,39}. When frequency shift is used as the detection scheme, the resonance frequencies of each vibration mode should be kept independent of each other (i.e., they should not interfere with each other), which can be achieved by modulating the coupling coefficient to 0. Furthermore, other than thermal strain, the introduction of the lattice mismatch strain may also an alternative method for tuning the mode

coupling coefficient⁴⁰, where the compressive strain is preloaded in the beam, thus eliminating the need for an additional heating system.

The theoretical model we established reveals the physical origin of the mode coupling coefficient in MEMS beam resonators. Different from the $N:1$ mode coupling^{41–43} that occurs only when the resonance frequencies of two vibrational modes fulfill or nearly fulfill with an integer ratio of N , mode coupling in this study is more generally present in an oscillating MEMS beam resonator, and originates from the interaction between the nonlinearities of two vibrational modes while two vibrational modes coupled to each other through the transfer of coherent energy in the case of the $N:1$ mode coupling. As shown in Fig. 3(b), the measured λ_{kj} is slightly perturbed when 3:1 mode coupling occurs, but it does not affect its overall trend as predicted by the theoretical model. This suggests the physical origin of the $N:1$ mode coupling may not be exact the same to that of the presented mode coupling in this study, which calls for further investigation. Nevertheless, the theoretical analysis provides valuable insight into the control of mode coupling coefficient. In terms of design strategies for a doubly-clamped beam structure: a smaller initial center deflection is preferable for achieving a large mode coupling coefficient using strain tuning. For a smaller mode coupling coefficient, the MEMS beam should be operated near its buckling point.

In conclusion, we have studied the mechanical mode coupling between two out-of-plane vibrational modes of an asymmetric doubly-clamped MEMS beam resonator. Mode coupling between out-of-plane modes originates from the oscillation-induced stiffness change in the beam, which provides the possibility of tuning the coupling coefficients through thermal strain. We estimated the coupling coefficients at various heating powers by measuring the resonance frequency of one mode as a function of the oscillation amplitude of the other mode. The experiment result

demonstrates that the coupling coefficients can be significantly tuned by thermal effect, which is promising for controlling the mode coupling strength in MEMS resonators to realize advanced sensing devices. A theoretical model is developed to quantitatively describe the coupling between two out-of-plane modes through the tension, and shows nice agreement with the measurements. The proposed model offers insights into fundamental principles of mode coupling in MEMS beam resonators, contributing to understanding mode coupling and the utilization of mode coupling in practical applications.

Materials and methods

Fabrication

As shown in Fig. 5 (a), the fabrication of the device starts from growing a 200-nm-thick GaAs buffer layer and a 3- μm -thick $\text{Al}_{0.7}\text{Ga}_{0.3}\text{As}$ sacrificial layer on a (100)-oriented GaAs substrate. The beam layer was formed by depositing a GaAs/ $\text{Al}_{0.3}\text{Ga}_{0.7}\text{As}$ superlattice buffer layer and a 1- μm -thick GaAs layer. We subsequently we formed a 2-dimensional electron gas (2DEG) layer by growing a 70-nm-thick $n^+\text{Al}_{0.3}\text{Ga}_{0.7}\text{As}$ layer and a 10-nm-thick undoped GaAs capping layer. Figure 5 (b) shows the schematic structure of the fabricated doubly clamped MEMS beam. The suspended beam with dimensions of $133\ \mu\text{m}(L)\times 27\ \mu\text{m}(b)\times 1\ \mu\text{m}(h)$ is formed by selectively etching the sacrificial layer with diluted hydrofluoric acid (HF). The top gates (NiCr /Au:15/100 nm) on both ends of the beam together with the 2DEG layer form two piezoelectric capacitors C_1 and C_2 ^{30,31,33}, and a 15-nm-thick NiCr layer was deposited on the beam as a heater for generating thermal strain in the MEMS beam.

Experimental process

To detect the frequency shifts in the probe mode due to the excitation of the pump mode, i.e.,

mode coupling measurement between the pump and probe modes, we follow the detection scheme described in Ref²⁷. Specifically, we keep the probe mode at resonance and perform frequency sweep for the pump mode only, which can be realized by tracking the resonance frequency of the probe mode using a PLL while driving the pump mode into its oscillation simultaneously. The effective stiffness in the MEMS beam changes when the pump mode is excited, thus the change in the resonance frequency of the probe mode is observed. The above measurement process has been conducted again at various heating powers to investigate the mode coupling coefficient change by thermal tuning effect.

Theoretical model

As shown in Fig. 4 (a), the model consists of a doubly-clamped beam with an initial transverse displacement, $X_0(u)$, governed by⁴⁴

$$X_0(u) = x_0\phi_0(u) = -\frac{x_0}{2}\left(1 - \cos\frac{2\pi}{L}u\right), \quad (6)$$

where x_0 is the initial center deflection of the beam; $\phi_0(u)$ is the profile function of initial shape; u is the coordinate along the length of the beam. Given by this initial condition, the motion equation of the MEMS beam describing its transverse vibrations is governed by the adapted Euler-Bernoulli equation⁴⁵, as

$$\rho S \frac{\partial^2 X}{\partial t^2} = -EI \left(\frac{\partial^4 X}{\partial u^4} + \frac{d^4 X_0}{du^2} \right) + T \left(\frac{\partial^2 X}{\partial u^2} + \frac{d^2 X_0}{du^2} \right), \quad (7)$$

with the following boundary conditions:

$$X|_{u=0,L} = 0 \text{ and } \frac{\partial X}{\partial u}\Big|_{u=0,L} = 0, \quad (8)$$

where $X(u,t)$ is the dynamical displacement from the equilibrium during the oscillation; t is the time scale; ρ is the density; E is the Young's modulus; L is the beam length; S and I denote the cross-section

area and the moment of inertia ($S=bh$ and $I=bh^3/12$ for beams of rectangular cross-sections, with b and h being the width and thickness of the MEMS beam, respectively); T is the tension in the MEMS beam ($T= T_0+\Delta T$), consisting of its inherent tension T_0 and the additional tension ΔT coming from the extension of the beam length (ΔL) in vibrations, written as

$$\Delta T = ES \frac{\Delta L}{L} = \frac{ES}{2L} \int_0^L \left[\left(\frac{\partial X}{\partial u} \right)^2 + 2 \frac{\partial X}{\partial u} \frac{dX_0}{du} \right] du. \quad (9)$$

Generally, the dynamical displacement of the beam is composed of different modes, for each mode, the displacement field can be expressed as the product of the mode shape function, $\phi(u)$, and the central displacement of the beam, $x(t)$, as

$$X(u, t) = \sum_n x_n(t) \phi_n(u). \quad (10)$$

The mode shape functions employed in this study are quoted from Ref. ³⁷. Then, substituting Eqs. (9) and (10) into Eq. (7), we can obtain:

$$\sum_{n=j,k} \rho S \phi_n \frac{\partial^2 x_n}{\partial t^2} = \sum_{n=j,k} -EI x_n \frac{\partial^4 \phi_n}{\partial u^4} - EI x_0 \frac{\partial^4 \phi_0}{\partial u^4} + \left(\sum_{n=j,k} x_n \frac{\partial^2 \phi_n}{\partial u^2} + x_0 \frac{d^2 \phi_0}{du^2} \right) \left(T_0 + \frac{ES}{2L} \sum_{m=j,k} \int_0^L \left[\left(x_m \frac{\partial \phi_m}{\partial u} \right)^2 + 2x_0 x_m \frac{\partial \phi_m}{\partial u} \frac{\partial \phi_0}{\partial u} \right] du \right), \quad (11)$$

where, we assume that there are at most two modes ($m, n = j, k$) excited on the beam, where mode- j is the pump mode and mode- k is the probe mode. We multiply $\phi_k(u)$ to both sides of Eq. (11) and then integrate it over beam length. Reorganizing the equation in the form of a duffing equation, we can obtain a motion equation for the MEMS beam (The processing is detailed in Appendix A), as

$$\ddot{x}_k + \left(\frac{EI}{\rho S L^4} \beta_k^4 + \frac{T_0 W_{kk}}{\rho S L^2} + \frac{x_0^2 E}{\rho L^4} W_{0k}^2 + \frac{E W_{kk} W_{jj}}{2 \rho L^4} x_j^2 \right) x_k + \left(\frac{3x_0 E}{2 \rho L^4} W_{kk} W_{0k} \right) x_k^2 + \left(\frac{E}{2 \rho L^4} W_{kk}^2 \right) x_k^3 + \left(\frac{x_0 E}{2 \rho L^4} W_{jj} W_{0k} \right) x_j^2 + \frac{T_0 W_{0k}}{\rho S L^2} x_0 + \frac{EI \beta_0^4}{\rho S L^4} x_0 \int_0^1 \phi_0 \phi_k du = 0. \quad (12)$$

This equation describes how the motion of mode- k affected by the excitation of mode- j (the terms containing x_j^2), as well as its own nonlinearity (the terms containing x_k^2 and x_k^3). W_{mn} a numerical value that computes the overlap between derivatives of the mode shapes. The effect of nonlinearity of a single vibrational mode has been reported in our previous work²⁸, and we here focus on the interaction between two vibrational modes. Since the steady-state equation holds for any new equilibrium position caused by the applied strain, the last two terms in Eq. (12) can be eliminated by replacing x_0 appearing in the other terms with a strain-induced center deflection, x_T , which can be expressed as

$$x_T = \frac{\frac{EI\beta_0^4}{L^4} \int_0^L (\phi_0)^2 du}{\frac{EI\beta_0^4}{L^4} \int_0^L (\phi_0)^2 du + \frac{T_0 W_{00}}{L}} x_0. \quad (13)$$

Then Eq. (12) becomes

$$\ddot{x}_k + (\omega_k^2 + D_1)x_k + \alpha_{2k}x_k^2 + \alpha_{3k}x_k^3 + D_2 = 0 \quad (14)$$

where $\omega_k = \sqrt{\frac{EI}{\rho SL^4} \beta_k^4 + \frac{T_0 W_{kk}}{\rho SL^2} + \frac{x_T^2 E}{\rho L^4} W_{0k}^2}$ is the resonance frequency of mode- k , $\alpha_{2k} = \frac{3x_T E}{2\rho L^4} W_{kk} W_{0k}$ is the quadratic nonlinearity coefficient, $\alpha_{3k} = \frac{E}{2\rho L^4} W_{kk}^2$ is the cubic nonlinearity coefficient, in the same spirit, $\alpha_{3j} = \frac{E}{2\rho L^4} W_{jj}^2$ for the cubic nonlinearity coefficient of mode- j . $D_1 = \frac{E W_{kk} W_{jj} a_j^2}{2\rho L^4}$ and $D_2 = \frac{x_T E}{2\rho L^4} W_{jj} W_{0k} \frac{a_j^2}{2}$ are the terms with respect to the oscillation amplitude of mode- j that affect the dynamical behavior of mode- k . Here, we use a harmonic approximation for x_j^2 , as $x_j = a_j \cos(\omega_j t)$, and then take time-averaged values over the oscillation cycles, yielding $x_j^2 = \frac{a_j^2}{2}$.

Next, we take a solution of the form for Eq. (14), as

$$x_k = \frac{1}{2} \left(a_k e^{i\omega_k' t} + \bar{a}_k e^{-i\omega_k' t} \right) + \delta, \quad (15)$$

where a_k indicates the oscillation amplitude of mode- k and the overbar indicates the complex

conjugate, ω_k' indicates the driving frequency (resonance frequency with excitation) of mode- k , and δ is a perturbed parameter given by D_1 and D_2 . By substituting Eq. (15) into Eq. (14), dropping terms in higher order of δ , and then matching the terms in $e^{i\omega_k't}$ and constant terms, respectively, this yields the following two equations,

$$-\omega_k'^2 + \omega_k^2 + D_1 + \frac{3}{4}\alpha_{3k}a_k^2 + 2\beta\delta = 0, \quad (16)$$

$$\delta\omega_k^2 + \delta D_1 + \frac{3}{2}\delta\alpha_{3k}a_k^2 + \frac{1}{2}\alpha_{2k}a_k^2 + D_2 = 0. \quad (17)$$

From Eq. (17) we can obtain:

$$\delta = \frac{-\frac{1}{2}\alpha_{2k}a_k^2 - D_2}{\omega_k^2 + D_1 + \frac{3}{2}\alpha_{3k}a_k^2}, \quad (18)$$

in which $D_1 + \frac{3}{2}\alpha_{3k}a_k^2$ can be ignored since it is a much smaller value compared to ω_k^2 , the Eq. (18) thus can be written as

$$\delta = \frac{-\frac{1}{2}\alpha_{2k}a_k^2 - D_2}{\omega_k^2}. \quad (19)$$

Then by substituting Eq. (19) into Eq. (16), yields

$$\omega_k'^2 = \omega_k^2 + D_1 + \frac{3}{4}\alpha_{3k}a_k^2 - \frac{\alpha_{2k}^2a_k^2 + 2\alpha_{2k}D_2}{\omega_k^2}, \quad (20)$$

Dividing both sides of Eq. (20) by ω_k^2 , and then taking the square root, yields

$$\frac{\omega_k'}{\omega_k} = \sqrt{1 + \frac{D_1}{\omega_k^2} + \frac{3\alpha_{3k}}{4\omega_k^2}a_k^2 - \frac{\alpha_{2k}^2a_k^2}{\omega_k^4} - \frac{2\alpha_{2k}D_2}{\omega_k^4}} \quad (21)$$

We apply Taylor expansion to Eq. (21) and drop the higher order terms, we can obtain:

$$\omega_k' = \omega_k \left[1 + \left(\frac{3\alpha_{3k}}{8\omega_k^2} - \frac{\alpha_{2k}^2}{2\omega_k^4} \right) a_k^2 + \left(\frac{EW_{kk}W_{jj}}{8\rho L^4\omega_k^2} - \frac{\alpha_{2k}x_T EW_{jj}W_{0k}}{4\rho L^4\omega_k^4} \right) a_j^2 \right]. \quad (22)$$

This equation shows the frequency shift of mode- k ($\Delta\omega = \omega_k' - \omega_k$) as a function of the oscillation

amplitudes of the two modes (a_j and a_k), in which $Y_{(\alpha_{2k}, \alpha_{3k})} = \frac{3\alpha_{3k}}{8\omega_k^2} - \frac{\alpha_{2k}^2}{2\omega_k^4}$ and $\lambda_{kj} = \frac{EW_{kk}W_{jj}}{8\rho L^4\omega_k^2} - \frac{\alpha_{2k}x_T EW_{jj}W_{0k}}{4\rho L^4\omega_k^4}$ represent the nonlinearity coefficient of mode- k and the mode coupling coefficient between mode- k and mode- j , respectively. When the probe mode is operated under a low excitation, the frequency shift contributed by the a_k is negligible, thus Eq. (22) can be further simplified as

$$\omega'_k - \omega_k = \omega_k \lambda_{kj} a_j^2. \quad (23)$$

Appendix A. Derivation details for Eq. (12)

We start from Eq. (11) with considering it multiplied by $\phi_k(u)$ and integrated over beam length, and then process it one by one. The term on the left side of the equal sign is written as

$$\sum_{n=j,k} \int_0^L \rho S \phi_n \frac{\partial^2 x_n}{\partial t^2} \phi_k du = \int_0^L \rho S \phi_j \frac{\partial^2 x_j}{\partial t^2} \phi_k du + \int_0^L \rho S \phi_k \frac{\partial^2 x_k}{\partial t^2} \phi_k du. \quad (A1)$$

Following the orthonormality for flexural modes of a beam³⁷: $\int_0^L \phi_j \phi_k du = 0$ ($j \neq k$) and

$\int_0^L \phi_j \phi_k du = L$ ($j = k$), Eq. (A1) yields:

$$\sum_{n=j,k} \int_0^L \rho S \phi_n \frac{\partial^2 x_n}{\partial t^2} \phi_k du = \rho S L \ddot{x}_k. \quad (A2)$$

By using the orthonormality condition and $\frac{\partial^4 \phi_n}{\partial u^4} = \frac{\beta_n^4}{L^4} \phi_n$, the first two terms on the right side of the equal sign can be expressed as

$$\sum_{n=j,k} \int_0^L -EI x_n \frac{\partial^4 \phi_n}{\partial u^4} \phi_k du - \int_0^L EI x_0 \frac{\partial^4 \phi_0}{\partial u^4} \phi_k du = -\frac{EI \beta_k^4}{L^3} x_k - \frac{EI \beta_0^4}{L^3} x_0 \int_0^1 \phi_0 \phi_k du, \quad (A3)$$

where $\beta_n = \{4.73, 7.8532, 10.996, 14.1372, \dots\}$ for $n=1,2,3,4\dots$ and $\beta_0 = 4.73$.

To be cautious, here, we decompose the remaining parenthesized multiplication term into 4 terms, and process them one by one. The two terms containing T_0 using integration by parts can be simplified as,

$$\begin{aligned} \int_0^L T_0 \sum_{n=j,k} x_n \frac{\partial^2 \phi_n}{\partial u^2} \phi_k du &= \sum_{n=j,k} T_0 x_n \left(- \int_0^L \frac{\partial \phi_n}{\partial u} \frac{\partial \phi_k}{\partial u} du + \phi_k \frac{\partial \phi_n}{\partial u} \Big|_{(0,L)} \right) \\ &= -\frac{T_0}{L} x_j W_{jk} - \frac{T_0}{L} x_k W_{kk} \end{aligned} \quad (A4)$$

$$\int_0^L T_0 \sum_{n=j,k} x_0 \frac{d^2 \phi_0}{du^2} \phi_k du = -\frac{T_0 x_0}{L} W_{0k}, \quad (A5)$$

where $\phi_k \frac{\partial \phi_n}{\partial u} \Big|_{(0,L)} = 0$ due to the boundary conditions as shown in Eq. (3) and $W_{nk} = \int_0^1 \frac{\partial \phi_n}{\partial u} \frac{\partial \phi_k}{\partial u} du$ ($n = 0, j, k \dots$). Surely, similar processing is performed in Eq. (A5). Next, we turn attention to the last two terms as shown in Eqs. (A6) and (A7).

$$\sum_{n=j,k} \int_0^L x_n \frac{\partial^2 \phi_n}{\partial u^2} \phi_k du \times \frac{ES}{2L} \sum_{m=j,k} \left\{ \int_0^L \left[\left(x_m \frac{\partial \phi_m}{\partial u} \right)^2 + 2x_0 x_m \frac{\partial \phi_m}{\partial u} \frac{\partial \phi_0}{\partial u} \right] du \right\} \quad (A6)$$

$$\int_0^L x_0 \frac{d^2 \phi_0}{du^2} \phi_k du \frac{ES}{2L} \sum_{m=j,k} \left\{ \int_0^L \left[\left(x_m(t) \frac{\partial \phi_m}{\partial u} \right)^2 + 2x_0 x_m(t) \frac{\partial \phi_m}{\partial u} \frac{\partial \phi_0}{\partial u} \right] du \right\}. \quad (A7)$$

In Eq. (A6), The integral to the left of the multiplication sign can be simplified using integrals by parts, referring to Eq. (A4), as

$$\sum_{n=j,k} \int_0^L x_n \frac{\partial^2 \phi_n}{\partial u^2} \phi_k du = -\frac{1}{L} (x_j W_{jk} + x_k W_{kk}). \quad (A8)$$

The part to the right of the multiplication sign in Eq. (A6) can be expressed as

$$\begin{aligned} &\frac{ES}{2L} \sum_{m=j,k} \left\{ \int_0^L \left[\left(x_m \frac{\partial \phi_m}{\partial u} \right)^2 + 2x_0 x_m \frac{\partial \phi_m}{\partial u} \frac{\partial \phi_0}{\partial u} \right] du \right\} \\ &= \frac{ES}{2L} \times \left[\frac{2x_0}{L} (x_j W_{0j} + x_k W_{0k}) + \frac{(x_j^2 W_{jj} + 2x_j x_k W_{jk} + x_k^2 W_{kk})}{L} \right] \end{aligned} \quad (A9)$$

Combining Eq. (A8) and Eq. (A9) in Eq. (A6), and then reorganizing the terms with decreasing order in x_k yields

$$-\frac{ES}{2L^3} \left[\begin{array}{c} x_k^3 W_{kk}^2 + x_k^2 (2x_0 W_{kk} W_{0k} + 3x_j W_{kk} W_{jk}) \\ + x_k (2x_0 x_j W_{jk} W_{0k} + 2x_j^2 W_{jk}^2 + x_j^2 W_{kk} W_{jj} + 2x_0 x_j W_{kk} W_{0j}) \\ + x_j^3 W_{jj} W_{jk} + 2x_0 x_j^2 W_{jk} W_{0j} \end{array} \right]. \quad (\text{A10})$$

With the similar processing performed to Eq (A7), it eventually can be expressed as

$$-\frac{ES}{2L^3} [x_k^2 x_0 W_{kk} W_{0k} + x_k (2x_0^2 W_{0k}^2 + 2x_0 x_j W_{0k} W_{jk}) + x_j^2 x_0 W_{jj} W_{0k} + 2x_j x_0^2 W_{0j} W_{0k}]. \quad (\text{A11})$$

Finally, we combine Eqs. (A2-A5) and (A10-A11) to form the equation of motion for the beam. It is

worth noting that, $W_{nk} = \int_0^1 \frac{\partial \phi_n}{\partial u} \frac{\partial \phi_k}{\partial u} du = 0$ when ϕ_n and ϕ_k have different parity. Here, we assume that mode- k (ϕ_k) is an even mode and mode- j (ϕ_j) is an odd mode. Since we know that the initial shape (ϕ_0) is an even mode, this results in $W_{jk} = 0$ and $W_{0j} = 0$. Substituting this result into the equation of motion for the beam, we can finally facilitate the expression as Eq. (12).

Appendix B. Calibration of the initial center deflection

The initial center deflection (x_0) of the MEMS beam resonator is attributed to factors such as the beam structure and the plastic deformation during the fabrication. In this work, the mesa structures at the two ends of the beam as illustrated in Fig. 5(b), predominantly contribute to the x_0 . Due to the existence of the mesa structure, the axis of the whole beam is no longer a horizontal straight line, resulting in an initial deflection. However, the x_0 does not exactly equal to the thickness of the mesa structure. such an exact equivalent x_0 can be calibrated by using buckling effect, as demonstrated in Ref.²⁸. Fig. A1 shows the resonance frequency of the 1st bending mode and the 2nd bending mode

(lines: theoretical calculation, circles: experimental data) as a function of heating power, P . As seen, considering both the buckling point and the frequency trend, the experimental data agrees with that of theoretical calculation at $x_0/h = 0.1$, indicating the equivalent x_0 is ~ 100 nm for the present MEMS beam resonators. Note that, the thermally induced strain used for the theoretical calculation can be expressed approximately as^{47,48}

$$\varepsilon_{th} = \frac{\alpha_T LP}{8G_T hb} \quad (\text{A12})$$

where α_T and G_T are the thermal expansion coefficient and the thermal conductivity of the MEMS beam, respectively. We can utilize the ε_{th} to calculate the inherent tension, T_0 (refer to Ref.²⁸), and further calculate the resonance frequency.

Appendix C. Excitation of 3:1 mode coupling

Strong internal ($N:1$) mode-coupling effect enables coherent energy transfer between two vibrational modes through the parametric driving effect^{49,50}, resulting in a sudden change in the resonance amplitude, as we have observed in our previous study³¹. For the present sample, the 3:1 mode coupling effect occurs at a nature frequency of 190 kHz in the probe mode and 569 kHz in the pump mode. Figure A2(a) shows the resonance spectrum (black) and phase (red) of the probe mode when it enters the nonlinear region, obtained by sweeping around 190 kHz. As seen, two clear drops are observed in the spectrum appear at 190 kHz, especially significant in the phase plot, suggesting the vibrational energy of the probe mode is reduced by the mode-coupling effect. One the other hand, Fig. A2(b) plots the oscillation amplitude of the pump mode as a function of its nature frequency modulated by heating power. As seen, the amplitude of the pump mode gradually decreases with the heating power due to the softening effect of the beam, but there is a sudden jump when its nature frequency is modulated to 569 kHz. This sudden jump corresponds to the drop appearing at 190 kHz

in the spectrum of the probe mode, indicating the probe mode coherently transfers its vibrational energy to the pump mode when the 3:1 mode coupling effect occurs and the amplitude of the pump mode is thereby enhanced.

References

1. Agrawal, D. K., Woodhouse, J. & Seshia, A. A. Observation of Locked Phase Dynamics and Enhanced Frequency Stability in Synchronized Micromechanical Oscillators. *Phys. Rev. Lett.* **111**, 084101 (2013).
2. Antonio, D., Zanette, D. H. & López, D. Frequency stabilization in nonlinear micromechanical oscillators. *Nat Commun* **3**, 806 (2012).
3. Qiao, Y. *et al.* Frequency unlocking-based MEMS bifurcation sensors. *Microsyst Nanoeng* **9**, 58 (2023).
4. Antonio, D. *et al.* Nonlinearity-Induced Synchronization Enhancement in Micromechanical Oscillators. *Phys. Rev. Lett.* **114**, 034103 (2015).
5. Shim, S.-B., Imboden, M. & Mohanty, P. Synchronized Oscillation in Coupled Nanomechanical Oscillators. *Science* **316**, 95–99 (2007).
6. Matheny, M. H. *et al.* Phase Synchronization of Two Anharmonic Nanomechanical Oscillators. *Phys. Rev. Lett.* **112**, 014101 (2014).
7. Chowdhury, A., Clerc, M. G., Barbay, S., Robert-Philip, I. & Braive, R. Weak signal enhancement by nonlinear resonance control in a forced nano-electromechanical resonator. *Nat Commun* **11**, 2400 (2020).
8. Madiot, G., Barbay, S. & Braive, R. Vibrational Resonance Amplification in a Thermo-Optic Optomechanical Nanocavity. *Nano Lett.* **21**, 8311–8316 (2021).

9. Chen, C., Zanette, D. H., Czaplewski, D. A., Shaw, S. & López, D. Direct observation of coherent energy transfer in nonlinear micromechanical oscillators. *Nat Commun* **8**, 15523 (2017).
10. Güttinger, J. *et al.* Energy-dependent path of dissipation in nanomechanical resonators. *Nature Nanotech* **12**, 631–636 (2017).
11. Mahboob, I. *et al.* Dispersive and Dissipative Coupling in a Micromechanical Resonator Embedded with a Nanomechanical Resonator. *Nano Lett.* **15**, 2312–2317 (2015).
12. Sharma, M., Sathyadharma Prasad, A., Freitag, N. H., Büchner, B. & Mühl, T. Coupled mechanical oscillator enables precise detection of nanowire flexural vibrations. *Commun Phys* **6**, 352 (2023).
13. Nathamgari, S. S. P. *et al.* Nonlinear Mode Coupling and One-to-One Internal Resonances in a Monolayer WS₂ Nanoresonator. *Nano Lett.* **19**, 4052–4059 (2019).
14. Wang, X., Wei, X., Pu, D. & Huan, R. Single-electron detection utilizing coupled nonlinear microresonators. *Microsyst Nanoeng* **6**, 78 (2020).
15. Zhang, M.-N., Dong, L., Wang, L.-F. & Huang, Q.-A. Exceptional points enhance sensing in silicon micromechanical resonators. *Microsyst Nanoeng* **10**, 12 (2024).
16. Verhagen, E., Deléglise, S., Weis, S., Schliesser, A. & Kippenberg, T. J. Quantum-coherent coupling of a mechanical oscillator to an optical cavity mode. *Nature* **482**, 63–67 (2012).
17. Deng, G.-W. *et al.* Strongly Coupled Nanotube Electromechanical Resonators. *Nano Lett.* **16**, 5456–5462 (2016).
18. Okamoto, H. *et al.* Coherent phonon manipulation in coupled mechanical resonators. *Nature Phys* **9**, 480–484 (2013).
19. Mahboob, I., Nishiguchi, K., Okamoto, H. & Yamaguchi, H. Phonon-cavity electromechanics. *Nature Phys* **8**, 387–392 (2012).

20. Zhou, X. *et al.* Dynamic modulation of modal coupling in microelectromechanical gyroscopic ring resonators. *Nat Commun* **10**, 4980 (2019).
21. Matheny, M. H., Villanueva, L. G., Karabalin, R. B., Sader, J. E. & Roukes, M. L. Nonlinear Mode-Coupling in Nanomechanical Systems. *Nano Lett.* **13**, 1622–1626 (2013).
22. Westra, H. J. R., Poot, M., van der Zant, H. S. J. & Venstra, W. J. Nonlinear Modal Interactions in Clamped-Clamped Mechanical Resonators. *Phys. Rev. Lett.* **105**, 117205 (2010).
23. Younis, M. I. & Nayfeh, A. H. A Study of the Nonlinear Response of a Resonant Microbeam to an Electric Actuation. *Nonlinear Dynamics* **31**, 91–117 (2003).
24. Li, L., Zhang, Q., Wang, W. & Han, J. Nonlinear coupled vibration of electrostatically actuated clamped–clamped microbeams under higher-order modes excitation. *Nonlinear Dyn* **90**, 1593–1606 (2017).
25. Faust, T. *et al.* Nonadiabatic Dynamics of Two Strongly Coupled Nanomechanical Resonator Modes. *Phys. Rev. Lett.* **109**, 037205 (2012).
26. Eichler, A., del Álamo Ruiz, M., Plaza, J. A. & Bachtold, A. Strong Coupling between Mechanical Modes in a Nanotube Resonator. *Phys. Rev. Lett.* **109**, 025503 (2012).
27. Arı, A. B., Çağatay Karakan, M., Yanık, C., Kaya, İ. İ. & Selim Hanay, M. Intermodal Coupling as a Probe for Detecting Nanomechanical Modes. *Phys. Rev. Appl.* **9**, 034024 (2018).
28. Li, C., Qiu, B., Yoshioka, Y., Hirakawa, K. & Zhang, Y. Mechanical Control of Nonlinearity in Doubly Clamped MEMS Beam Resonators Using Preloaded Lattice-Mismatch Strain. *Physical Review Applied* **19**, 024025 (2023).
29. Zhang, Y. *et al.* Thermal tuning of mechanical nonlinearity in GaAs doubly-clamped MEMS beam resonators. *Applied Physics Letters* **119**, 163503 (2021).
30. Zhang, Y., Watanabe, Y., Hosono, S., Nagai, N. & Hirakawa, K. Room temperature, very sensitive thermometer using a doubly clamped microelectromechanical beam resonator for

bolometer applications. *Appl. Phys. Lett.* **108**, 163503 (2016).

31. Zhang, Y., Kondo, R., Qiu, B., Liu, X. & Hirakawa, K. Giant Enhancement in the Thermal Responsivity of Microelectromechanical Resonators by Internal Mode Coupling. *Phys. Rev. Applied* **14**, 014019 (2020).

32. Mahboob, I. & Yamaguchi, H. Bit storage and bit flip operations in an electromechanical oscillator. *Nature Nanotech* **3**, 275–279 (2008).

33. Zhang, Y., Hosono, S., Nagai, N., Song, S.-H. & Hirakawa, K. Fast and sensitive bolometric terahertz detection at room temperature through thermomechanical transduction. *Journal of Applied Physics* **125**, 151602 (2019).

34. Ramini, A. H., Hajjaj, A. Z. & Younis, M. I. Tunable Resonators for Nonlinear Modal Interactions. *Sci Rep* **6**, 34717 (2016).

35. Asadi, K., Yeom, J. & Cho, H. Strong internal resonance in a nonlinear, asymmetric microbeam resonator. *Microsyst Nanoeng* **7**, 9 (2021).

36. Asadi, K., Yu, J. & Cho, H. Nonlinear couplings and energy transfers in micro- and nano-mechanical resonators: intermodal coupling, internal resonance and synchronization. *Phil. Trans. R. Soc. A.* **376**, 20170141 (2018).

37. Younis, M. I. *MEMS Linear and Nonlinear Statics and Dynamics*. (Springer Science & Business Media, 2011).

38. Olcum, S., Cermak, N., Wasserman, S. C. & Manalis, S. R. High-speed multiple-mode mass-sensing resolves dynamic nanoscale mass distributions. *Nat Commun* **6**, 7070 (2015).

39. Jaber, N., Ilyas, S., Shekhah, O., Eddaoudi, M. & Younis, M. I. Multimode MEMS Resonator for Simultaneous Sensing of Vapor Concentration and Temperature. *IEEE Sensors J.* **18**, 10145–10153 (2018).

40. Qiu, B., Zhang, Y., Nagai, N. & Hirakawa, K. Enhancing the thermal responsivity of

microelectromechanical system beam resonators by preloading a critical buckling strain. *Appl. Phys. Lett.* **119**, 153502 (2021).

41. Nathamgari, S. S. P. *et al.* Nonlinear Mode Coupling and One-to-One Internal Resonances in a Monolayer WS₂ Nanoresonator. *Nano Lett.* **19**, 4052–4059 (2019).

42. Pu, D., Wei, X., Xu, L., Jiang, Z. & Huan, R. Synchronization of electrically coupled micromechanical oscillators with a frequency ratio of 3:1. *Applied Physics Letters* **112**, 013503 (2018).

43. Samanta, C., Yasasvi Gangavarapu, P. R. & Naik, A. K. Nonlinear mode coupling and internal resonances in MoS₂ nanoelectromechanical system. *Applied Physics Letters* **107**, 173110 (2015).

44. Tella, S. A., Hajjaj, A. Z. & Younis, M. I. The Effects of Initial Rise and Axial Loads on MEMS Arches. *Journal of Vibration and Acoustics* **139**, 040905 (2017).

45. Lifshitz, R. & Cross, M. C. Nonlinear dynamics of nanomechanical and micromechanical resonators. *Reviews of nonlinear dynamics and complexity* **1**, (2008).

47. Zhang, Y., Hosono, S., Nagai, N. & Hirakawa, K. Effect of buckling on the thermal response of microelectromechanical beam resonators. *Appl. Phys. Lett.* **111**, 023504 (2017).

48. Qiu, B., Zhang, Y., Akahane, K., Nagai, N. & Hirakawa, K. Effect of beam deflection on the thermal responsivity of GaAs-based doubly clamped microelectromechanical beam resonators. *Appl. Phys. Lett.* **117**, 203503 (2020).

49. Yamaguchi, H. & Mahboob, I. Parametric mode mixing in asymmetric doubly clamped beam resonators. *New J. Phys.* **15**, 015023 (2013).

50. Yamaguchi, H. GaAs-based micro/nanomechanical resonators. *Semicond. Sci. Technol.* **32**, 103003 (2017).

Acknowledgments

We thank Dr. Isao Morohashi for the support in the device fabrication process. This work has been partly supported by the A-STEP program of JST, MEXT Grant-in-Aid for Scientific Research on Innovative Areas “Science of hybrid quantum systems” (15H05868), and KAKENHI from JSPS (21K04151, 24K00937).

Author contributions

Ya Zhang conceived the idea of the work. Chao Li designed and fabricated the device, and performed the experiments and data analysis. Qian Liu and Kohei Uchida supported the fabrication and measurement. The theoretical works were done by Chao Li. The manuscript was written by Chao Li, and revised by Ya Zhang. Hua Li and Kazuhiko Hirakawa discussed the results and commented on the manuscript.

Competing interests

The authors declare no competing interests.

Figures and captions

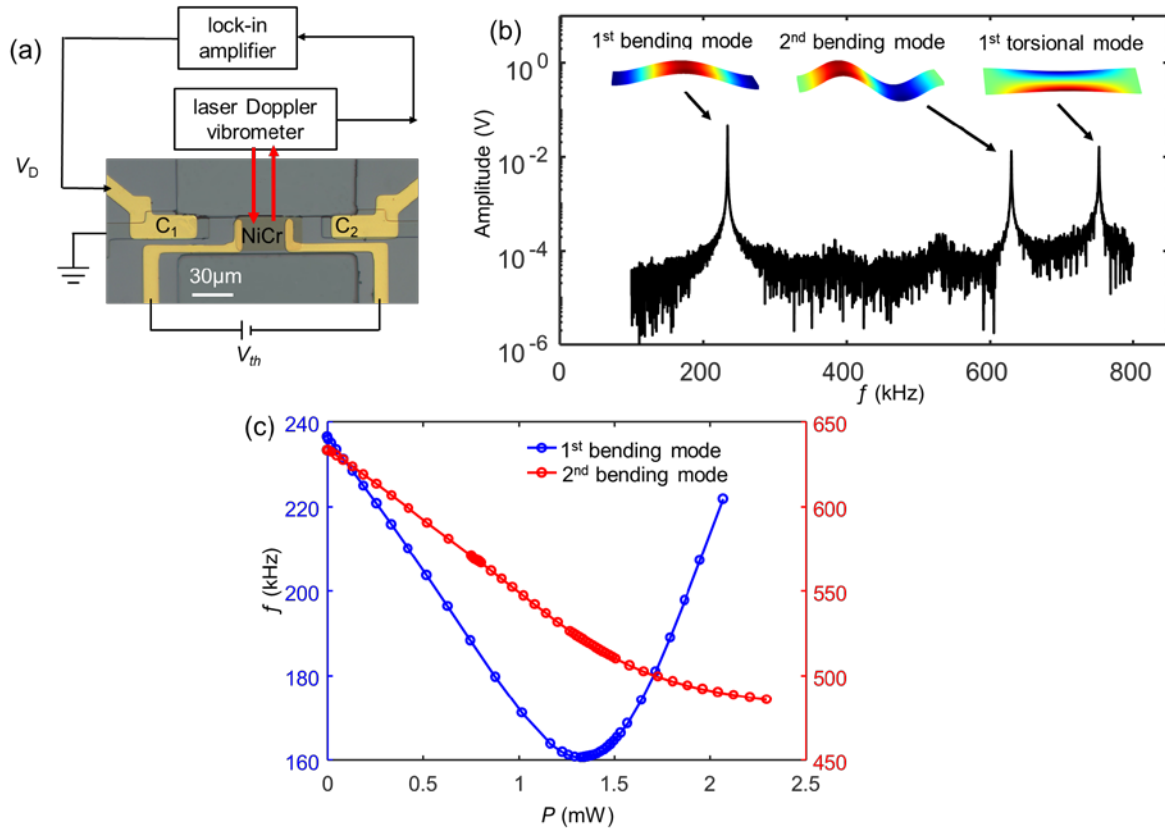


Figure 1 (a) A microscope image of fabricated MEMS beam resonator. An ac voltage (V_D) is applied to one of the piezoelectric capacitors to drive the resonator and the induced mechanical oscillation is measured by a laser Doppler vibrometer and a lock-in amplifier with a built-in PLL. A dc voltage (V_{th}) is applied to the NiCr film to generate heat in the beam. (b) Measured spectrum for the first three modes (i.e., the first bending mode, the second bending mode, and the first torsional mode). The upper insets show the mode shapes of the first three modes. (c) The measured resonance frequencies of the 1st bending mode (blue) and the 2nd bending mode (red) as a function of heating power, P . the 1st bending mode achieves its buckling at $P=1.33$ mW (160 kHz).

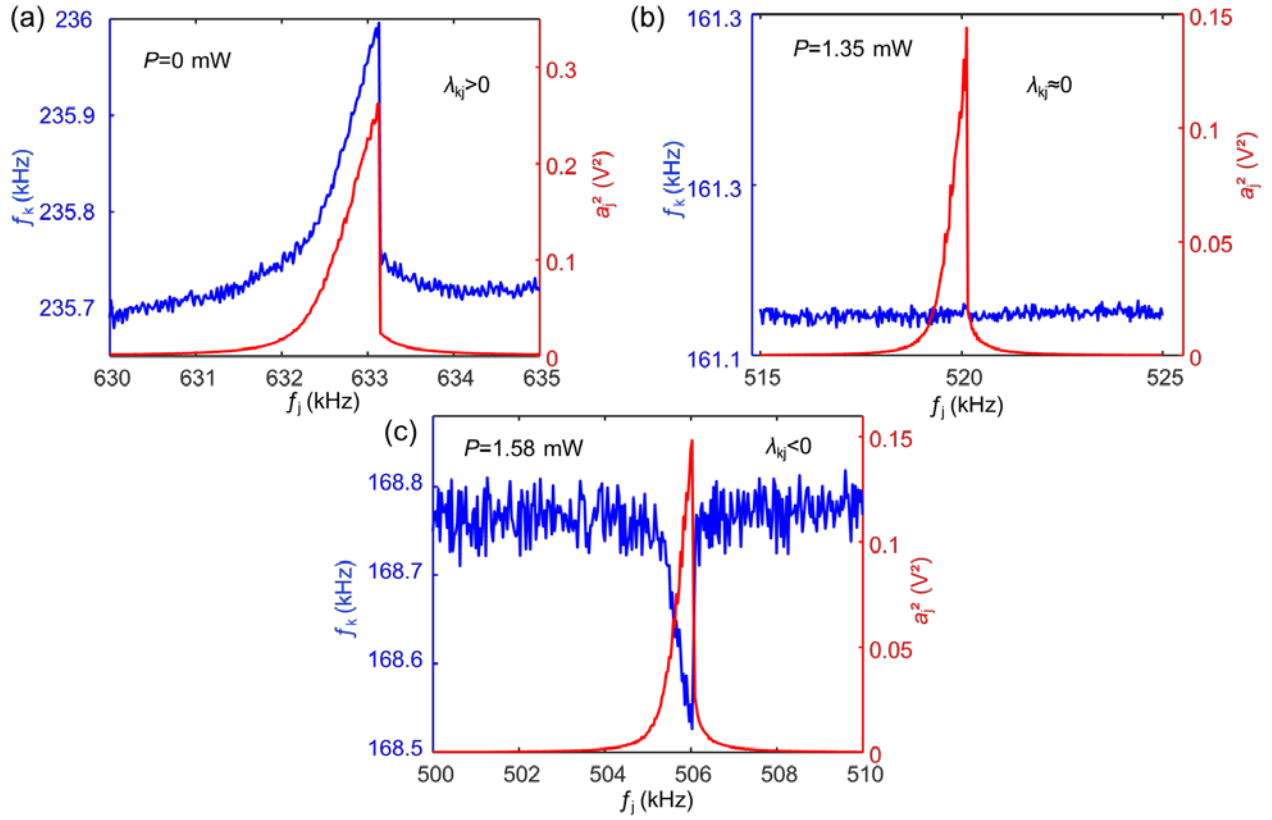


Figure 2 (a-c) PLL mode coupling measurements between the pump and probe modes, at various heating powers. The x-axis plots the driving frequency of the pump mode (f_j); the left y-axis plots the resonance frequency (f_k) of the probe mode traced by PLL, and the right y-axis plots the squared amplitude of the pump mode (a_j^2). (a-c) show the cases of $\lambda_{kj} > 0$, $\lambda_{kj} \approx 0$ and $\lambda_{kj} < 0$, respectively.

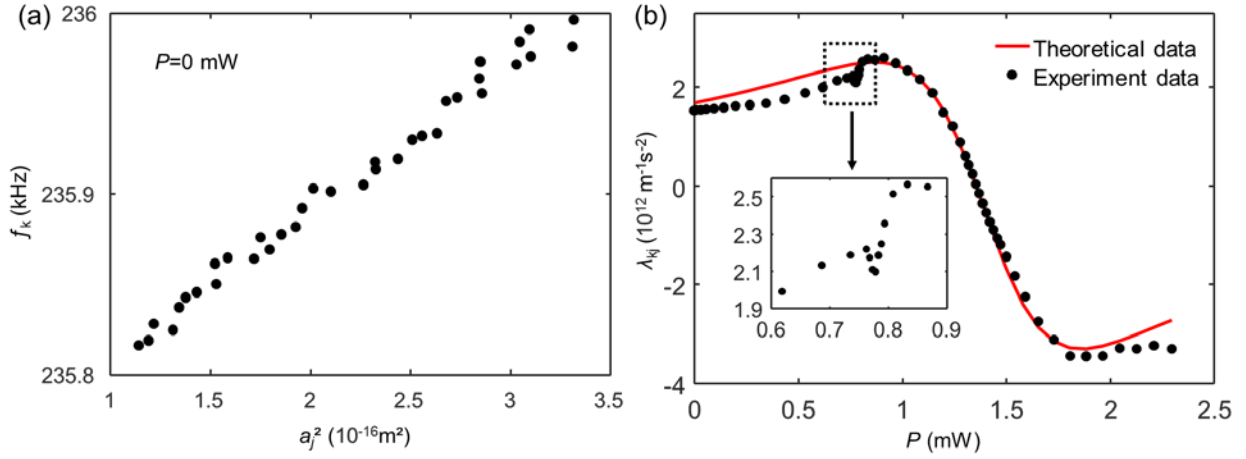


Figure 3 (a) The resonance frequency of probe mode (f_k) as a function of the squared amplitude of the pump mode (a_j^2) for the case of $P=0 \text{ mW}$, with the data of Fig. 2 (a) that larger than $\frac{\sqrt{3}}{3}$ of the maximum a_j . (b) the measured mode coupling coefficient, λ_{kj} , (dots) and calculated λ_{kj} (red line) as a function of heating power. The measured λ_{kj} is obtained by performing linear fitting based on Eq. (1). The inset is a magnification of the measured λ_{kj} (marked by the dotted black rectangle) near the 3:1 mode coupling point ($P=0.6\text{-}0.9 \text{ mW}$).

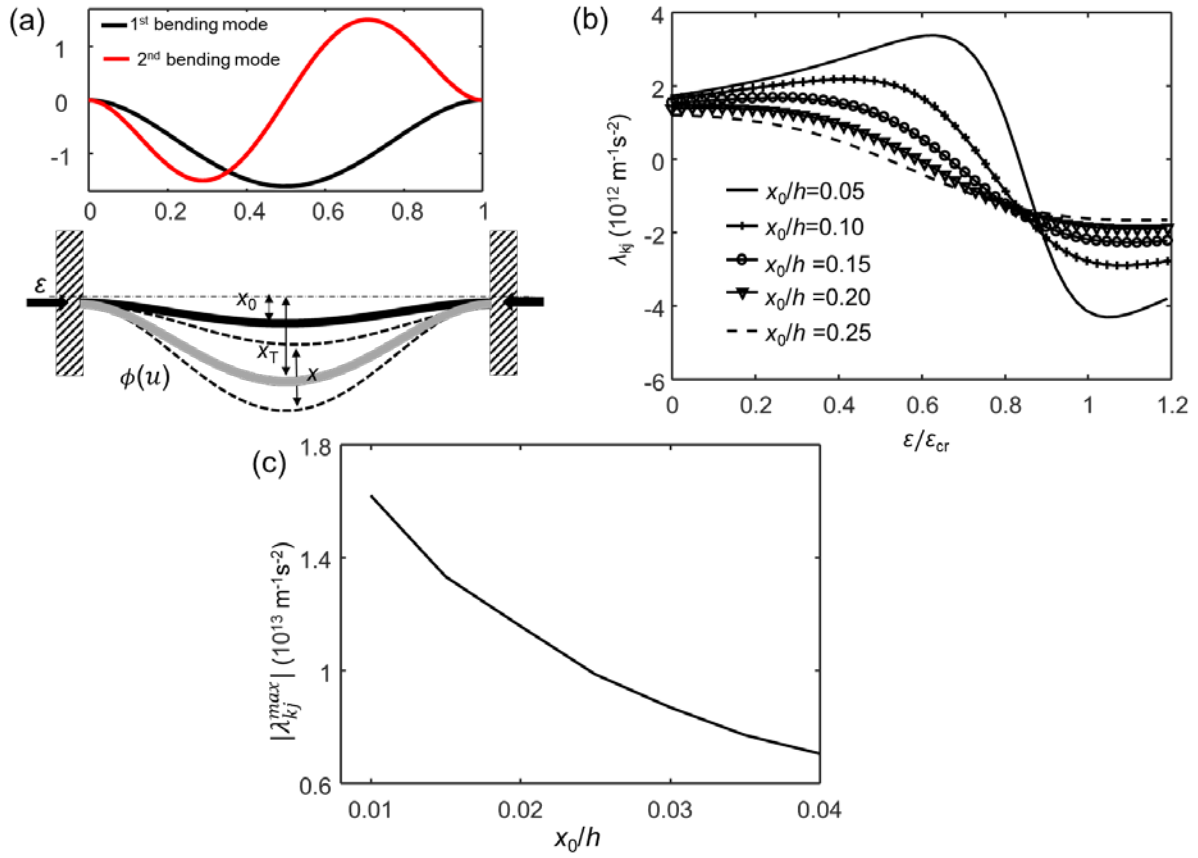


Figure 4 (a) Schematic diagram of a doubly-clamped MEMS beam with an initial center deflection. When the center deflection increases from x_0 to x_T , the MEMS beam has a new equilibrium position for the oscillation. The inset shows the 1-dimensional mode shapes of the 1st bending and 2nd bending modes. (b) The calculated mode coupling coefficient, λ_{kj} , as a function of the compressive strain ($\varepsilon/\varepsilon_{cr}$) at various initial center deflections ($x_0/h=0, 0.05, 0.10, 0.15, 0.20, 0.25$). ε is normalized by the Euler's buckling critical strain, ε_{cr} , of the MEMS beam. (c) The achievable maximum in the mode coupling coefficient ($|\lambda_{kj}^{max}|$) as a function of x_0/h .

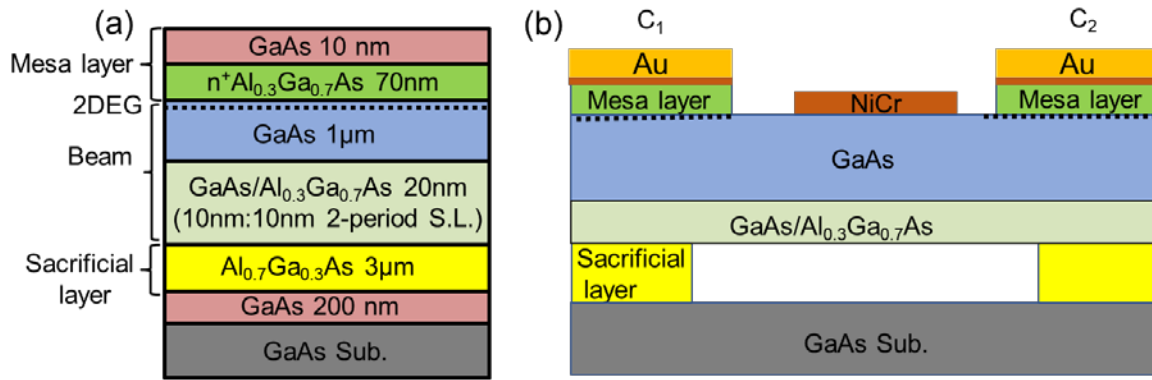


Figure 5 (a) The wafer structure used for fabricating the GaAs MEMS beam resonators. (b) Schematic structure of the fabricated doubly-clamped MEMS beam. The top gates (NiCr /Au:15/100 nm) on both ends of the beam together with the 2DEG layer form two piezoelectric capacitors, C_1 and C_2 . A 15-nm-thick NiCr layer was deposited as a heater.

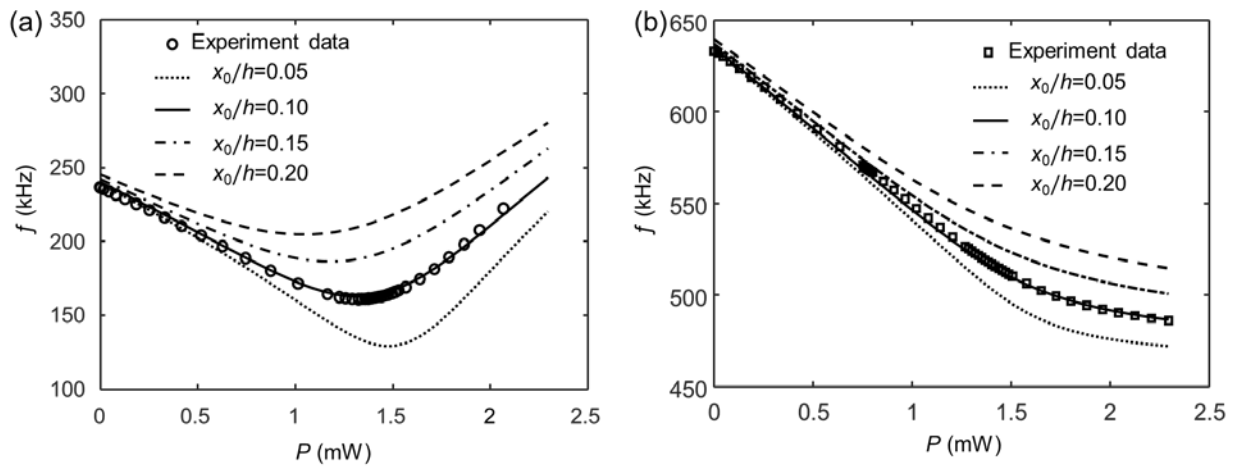


Figure A1 (a) The resonance frequency of the 1st bending mode as a function of heating power (lines: theoretical calculation, circles: experimental data), at various initial center deflection ($x_0/h=0, 0.05, 0.1, 0.15, 0.2$). (b) The resonance frequency of the 2nd bending mode as a function of heating power (lines: theoretical calculation, square: experimental data), at various initial center deflection ($x_0/h=0, 0.05, 0.1, 0.15, 0.2$).

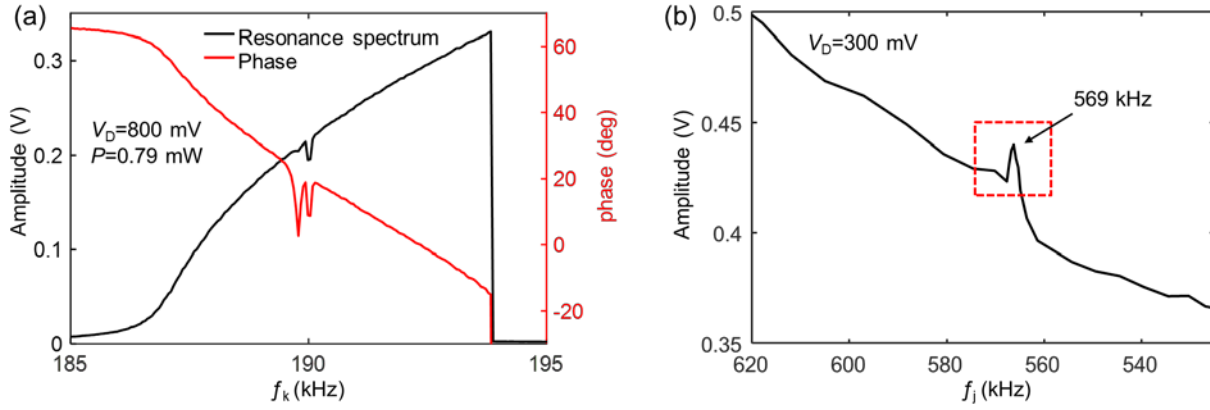


Figure A2 (a) The resonance spectrum and phase of the probe mode near 190 kHz, with a driving voltage of $V_D=800$ mV and a heating power of $P=0.79$ mW. Two clear drops in both spectrum and phase plots indicate the presence of 3:1 mode coupling. (b) The oscillation amplitude of the pump mode as a function of its nature frequency modulated by heating power. The sudden jump marked by the red dashed rectangle indicates the amplitude enhancement due to 3:1 mode coupling effect, corresponding to the drops in (a).